Marine Stratocumulus Structure

Robert F. Cahalan

Laboratory for Atmospheres, Goddard Space Flight Center

Jack B. Snider

NOAA / ERL / Wave Propagation Laboratory

*T*hirty-three Landsat TM scenes of California stratocumulus cloud fields were acquired as part of the FIRE Marine Stratocumulus Intensive Field Observations in July 1987. They exhibit a wide variety of stratocumulus structures. Analysis has so far focused upon the 7 July scene, in which aircraft from NASA, NCAR, and the British Meteorological Office repeatedly gathered data across a stratocumulus-fair weather cumulus transition. The aircraft soundings validate the cloud base temperature threshold determined by spatial coherence analysis of the TM thermal band. Brightness variations in the stratocumulus region exhibit a $-5/3$ power-law decrease of the wavenumber spectra for scales larger than the cloud thickness, about 200 m, changing to a -3 power at smaller scales. Observations by an upward-looking three-channel microwave radiometer on San Nicolas Island also show the $-5/3$ power-law in total integrated liquid water, suggesting that the larger-scale TM brightness variations are primarily due to variations in the liquid water. The Kolmogorov $5/3$ power suggests that for some purposes liquid water in turbulent stratocumulus clouds may be treated as a passive scalar, simply reflecting variations in vertical velocity. This may be tested using the velocities measured by the aircraft.

INTRODUCTION

This paper summarizes the fractal properties of clouds observed during the FIRE Marine Stratocumulus Intensive Field Observations (MS IFO) and their implications for the large-scale radiative properties of the atmosphere. FIRE is the First Regional Experiment of the International Satellite Cloud Climatology Project. Many theoretical studies have shown the sensitivity of cloud radiative properties to their spatial structure, ranging from the seminal work of McKee and Cox (1974) and Stephens (1976) to more recent work by Harshvardhan and Weinman (1982), Welch and Wielicki (1985), and others. Harshvardhan and Randall (1985) pointed out the embarrassing implications of plane-parallel assumptions for general circulation models, which must use unrealistically small liquid water amounts to produce realistic albedos, and Stephens (1985) has emphasized that the mean albedo is not a function of mean liquid water alone, but depends upon its spatial distribution. Cahalan (1989) discussed a simple fractal model,

showing that only liquid water variations on scales larger than the photon mean-free-path contribute to the albedo, smaller-scale changes being smoothed out by the transfer process.

Marine stratocumulus are perhaps closest to plane-parallel, being largely confined between the lifting condensation level and the strong subtropical inversion. Ohring and Clapp (1980) and Hartmann and Short (1980) dramatized the importance of marine stratocumulus for climate, showing that they are able to produce the largest increase in reflected radiation for a given small change in emitted radiation, giving a net cooling which could potentially mitigate the expected greenhouse heating. Cahalan and Joseph (1989) have determined the fractal properties of marine stratocumulus (as well as fair weather cumulus and deep cumulus) from Landsat data, as part of a program to compute their mean radiative properties by Monte Carlo techniques, and thus determine the errors associated with plane-parallel results. The purpose of the present paper is to compare the Landsat observations of cloud temperature and reflectivity with *in situ* observations of cloud temperature and liquid water during FIRE. The main new result is a change in the stratocumulus wavenumber spectrum from a $-5/3$ power to a -3 power at a scale determined by the cloud thickness, which we relate to theoretical work of Kraichnan (1967) and empirical work of Gage and Nastrom (1986).

The 1987 FIRE marine stratocumulus field experiment has been summarized by Albrecht et al. (1988). Surface, cloud, and atmospheric microphysical and radiation data were collected over a 3-week period at San Nicolas Island, and onboard an NSF ship, five aircraft (BMO C-130, NASA ER-2, NCAR Electra, UW C-131, and NOSC Piper Navaho), and seven satellites (DMSP, ERBS, GOES, Landsat-5, NOAA-9, NOAA-10, SPOT). The primary goal was to derive a consistent picture of the cloud structure from a variety of measurements over a wide range of scales of a cloud type which dominates the albedo of much of the earth's subtropical oceans, and therefore plays a significant role in determining the global energy budget and climate. Landsat's Thematic Mapper (TM) instrument was a key element in FIRE, providing a spatial resolution comparable to the aircraft, with a field of view approaching that of the meteorological satellites. Several TM scenes were operationally useful in coordinating multiple aircraft observations, and scientifically important

in focusing a number of separate investigations on the same cloud field. (SPOT provided important nonnadir high-resolution data in three scenes, including part of the 7 July TM scene analyzed in this paper. Its role was reduced somewhat by coordination problems and lack of a thermal channel.)

The outline of the paper is as follows: The next section summarizes the FIRE data used in this paper. The third section compares the surface, cloud base, and cloud top temperatures estimated from the Landsat TM with those observed by the NCAR Electra, and summarizes the fractal properties of the fair weather cumulus and stratocumulus cloud fields in the 7 July scene. The fourth section compares the wavenumber spectra determined from the TM reflectances with those determined from vertically integrated liquid water observed on San Nicolas Island. The fifth and final section summarizes the results and indicates directions for future work.

DATA

Before describing the TM data acquired during FIRE, we first summarize the two sources of *in situ* data used in the present study: the NCAR Electra temperature sensor used in the next section to verify the cloud base threshold, and the NOAA microwave radiometer used in the fourth section to relate the spatial structure observed by Landsat to that of integrated liquid water.

Aircraft and Island

The NCAR Electra measured water vapor concentration with top and bottom Cambridge dewpoint thermometers (DPTC AND DPBC) and a Lyman-α hygrometer (RHOLA). Temperature was measured by four probes: fast response (ATKP), reverse flow (ATRF), Rosemount (ATB), and radiometer (PRT6). Airspeed corrections are discussed in Miller and Freisen (1987), and corrections for the oscillatory and lagged response of the dewpoint sensors have been given by Boers and Betts (1988). The relative responses of the various instruments have been discussed by Austin and Boers (1988). Errors are generally less than 1 K. In this paper we use the fast-response temperature sensor and the top-mounted dewpoint thermometer.

Path integrated liquid water and precipitable water vapor were measured at 10 Hertz (Hz) and

averaged for 1 min by an upward-looking three-channel microwave radiometer (20.6, 31.65, and 90.0 Hz) on San Nicolas Island during 1–19 July 1987 (the FIRE MS IFO period). The accuracy of these measurements has been discussed by Snider (1988); the microwave radiometer is described in Hogg et al. (1983). The uncertainty in the absolute value of the radiometric liquid measurement is greatest at values below the 0.1 mm (100 g/m^2), and the smallest detectable value is about 0.02 mm. In this paper, we are concerned only with the

relative fluctuations, which are expected to be accurate to about 10%.

Landsat

Thirty-three Landsat TM scenes along six swaths over the eastern Pacific Ocean were acquired during the FIRE marine stratocumulus intensive field operations. Six of these, which were coincident with various *in situ* measurements, have been geometrically and radiometrically processed, and

Figure 1. NOAA-10 image of California stratocumulus at 1643 GMT on 7 July 1987. Shown are the water vapor window (Channel 4, 10.5–11.5 μm), the 3.7 μm solar infrared (Channel 3, 3.55–3.93 μm), and the visible (Channel 1, 0.58–0.68 μm). The apparently sharp boundary between the clear patch on the right side of the visible scene and the solid coastal stratocumulus appears at the center of the LANDSAT overpass at 1800 GMT. A number of ship tracks are evident in the more broken offshore stratocumulus. (Figure from Coakley and Beckner, 1988).
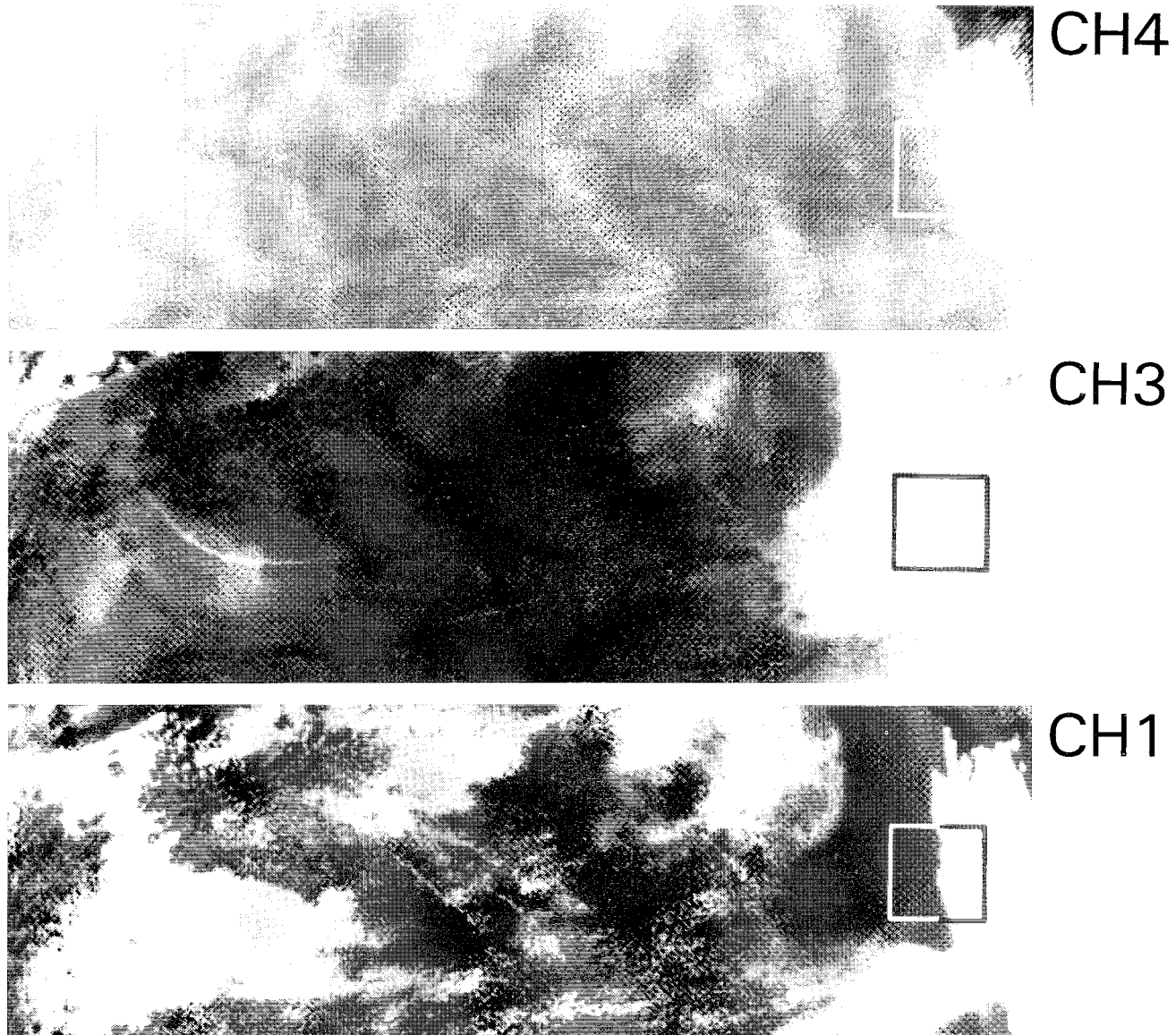
are available in machine-readable form. We focus in this paper on the 7 July case, in which the NASA ER-2, the BMO C-130, and the NCAR Electra repeatedly gathered data across a stratocumulus-fair weather cumulus transition.

The large-scale cloud pattern on 7 July may be seen in Fig. 1, which shows three channels of a NOAA-10 AVHRR scene acquired at 1643 GMT (9:43 am local time). The thermal band (Channel 4) shows a very uniform cloud-top temperature, while the near-infrared and visible reflected bands show patchy stratocumulus over most of the area. The right side of the visible band (Channel 1) shows apparently solid stratocumulus hugging the coast, and bounded on the ocean side by an apparently clear patch, with the interface between the two appearing quite sharp. This "clear–cloudy" interface occurs at the center of the Landsat overpass at 1800 GMT (11 am local). The solid square indicates the approximate region of cloud seen by Landsat. As we shall see, the "clear" region is actually filled with a large number of fair weather cumulus clouds, all well below AVHRR resolution. In addition, we shall see that in the stratocumulus region the Landsat TM reveals considerable spatial structure, again not resolved by the AVHRR.

Three aircraft gathered *in situ* data across the stratocumulus boundary within the Landsat area indicated in Fig. 1, using the Landsat TM center coordinates as a focal point. The center coordinates conveniently fell precisely in the stratocumulus-fair weather cumulus transition region. The TM scene boundary and aircraft flight tracks are shown in Fig. 2. The ER-2 flew a "racetrack" pattern at about 60,000 feet (the dashed curve in Fig. 2), while the BMO C-130 and the NCAR Electra flew in and just above the cloud layer. The Electra initially flew a "butterfly" pattern (the solid curve in Fig. 2), and then repeatedly traversed the transition region on east–west flight legs, as the stratocumulus boundary advected to the east.

Two 60×60 km (2048² pixel) subscenes, one in the fair weather cumulus and one in the stratocumulus, with boundaries labeled in Fig. 2 as "subscene a" and "subscene b," respectively, were chosen for analysis. The Band 7 (2.2 μm) subimages in Figs. 3a) and 3b), respectively, show considerable structure not observable in the AVHRR image. (The same structure is observed in Band 2, which is used for the numerical analysis, but the Band 7 image appears somewhat sharper because it has no saturation, and possibly because of its greater absorption.) Subscene a shows a large number of small fair weather cumulus clouds, with diameters typically less than 1/2 km, aligned in streets oriented parallel to the wind, and separated by about 1–2 km. Subscene b shows much larger

Figure 2. Boundary of the thematic mapper (TM) scene on 7 July 1987, and aircraft flight patterns at about the time of the LANDSAT overpass at 1800 GMT (11 am local). The stratocumulus boundary is about in the center of the scene, so that the two 60 km subscenes labelled 3a and 3b are on the clear and cloudy sides of the boundary referred to in Fig. 1. The boundary moved steadily eastward at about 60 kph, so that the Electra sounding shown in Fig. 5, taken across the boundary an hour later, was at the right edge of the TM scene.
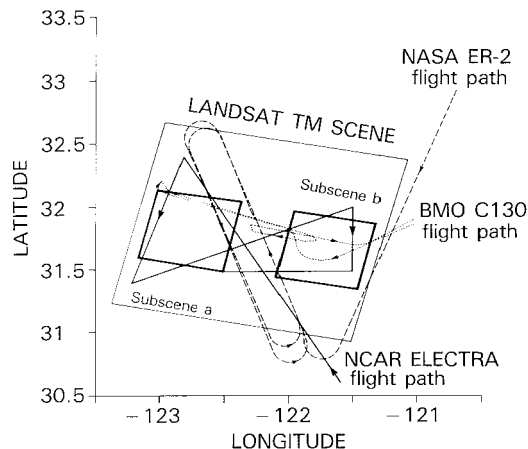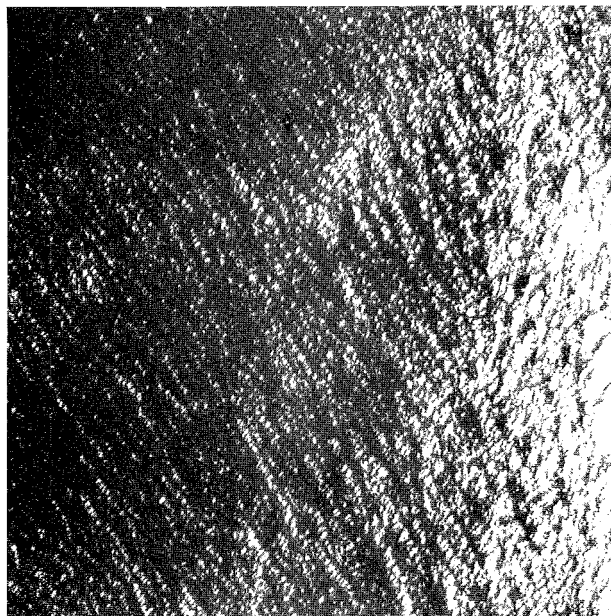

Figure 3a). TM (Band 7) fair weather cumulus subscene on 7 July 1987. The subscene boundaries are shown on the left side of Fig. 2. Note the cloud streets oriented parallel to the wind.
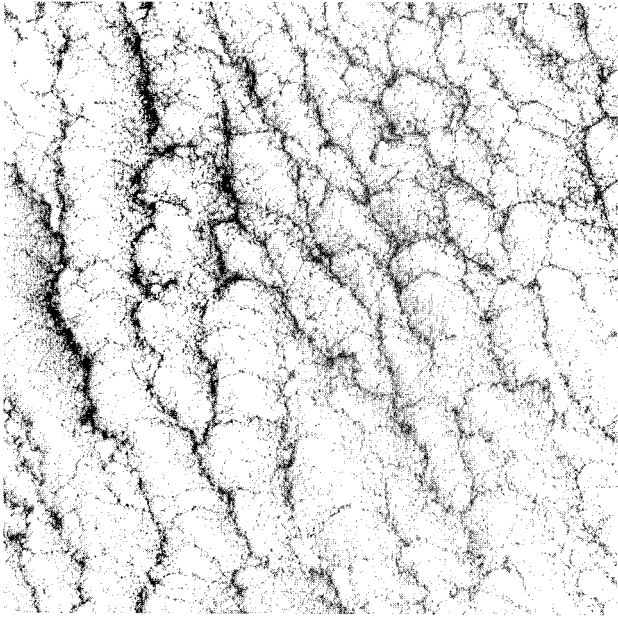
Figure 3b). TM (Band 7) stratocumulus subscene on 7 July 1987. The subscene boundaries are shown on the right side of Fig. 2. Note the cloud streets oriented parallel to the wind.

cells, again aligned parallel to the wind, in streets having about the same width as the cells, typically about 8 km. The 8 km streets reveal considerable structure on smaller scales, the whole subscene being covered by an intricate dark filigree. We shall see in the next section that this dendritic network of dark regions has a fractal boundary of dimension equal to 1.8, so that it nearly covers the two-dimensional area. In the fourth section we show that the larger-scale variability in this scene has the same wavenumber spectrum as the vertically integrated liquid water.

TM Brightness Histograms

The Landsat TM has three visible reflected bands, three near-infrared bands, and the thermal water vapor window band. The 7 July stratocumulus clouds have a maximum reflectance of about 0.5, which saturates two of the visible and one of the near-infrared TM bands. Table 1 shows the typical maximum reflectance required to saturate each band (using the 7 July zenith angle of 30°). Bands 1, 3, and 5 are all saturated at a reflectance of less than 0.5, and thus are saturated by the 7 July stratocumulus. Band 2 (0.52–0.60 μm) is saturated at 0.5, so that only the few brightest pixels are

Table 1. Landsat TM Reflected Bands with Nominal Wavelength Ranges and Maximum Reflectances

Band	Wavelength (μm)	R_{sat}	Saturated?
1	0.45–0.52	0.25	✓
2	0.52–0.60	0.58	
3	0.63–0.69	0.53	✓
4	0.76–0.90	0.73	
5	1.55–1.75	0.47	✓
7	2.08–2.35	0.69	

*Source:* From Clark (1986), corrected for solar zenith angle of 30°.

A check in the last column indicates that most cloud pixels are saturated, so that the gain settings of these bands are of limited use in cloud analysis.

saturated. Bands 4 and 7 are well below saturation.

The histogram of the thermal band (Band 6, 104–12.5 mμ) for a 15 km subscene at the stratocumulus edge is shown in Fig. 4a). The two narrow peaks, separated by about 5°C, correspond to the surface and cloud top. A dry adiabatic lapse rate (appropriate for subcloud) then estimates cloud top at about 500 m, while a moist rate (appropriate for in-cloud) would raise it to 800 m. According to the *in situ* sounding discussed in the next section, actual cloud top is at about 650 m, with cloud base at 400 m (and 3.9°C colder than the surface) and cloud top another 250 m above that (and 1.5°C colder).

Plots of temperature versus brightness (Band 6 vs. Band 7, for example) show the usual scatter of points extending up from the warm dark surface cluster to the cold bright cloud cluster. At 1 km resolution the points are all concentrated at the

Figure 4a). Histogram of TM thermal band (Band 6, 10.4–12.6 μm) for a 128^2 subscene in the transition region (between subscenes a and b). The low-temperature peak is associated with the cloud top, and the high-temperature one with the surface.
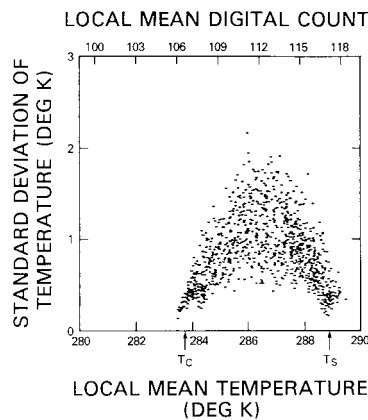
LOCAL MEAN DIGITAL COUNT
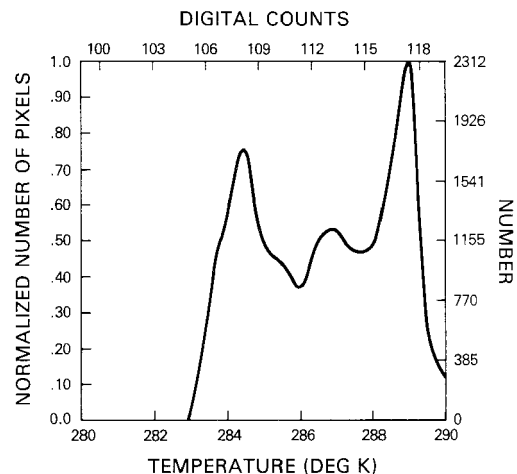
Figure 4b). Spatial coherence scatter plot of the same sub-scene used in Fig. 4a). Each point gives the mean and standard deviation of the temperature of a 4×4 pixel array. The two clusters of points having minimum standard deviation determine the cloud top temperature $T_c = 10.55°C$ and the surface temperature $T_s = 15.65°C$. If we assume that the temperature of the ith pixel array depends on its cloud fraction through $T(i) = A_c(i)T_c + [1 - A_c(i)]T_s$, then the mean cloud fraction may be determined from the mean temperature, giving $A_c = 45\%$.
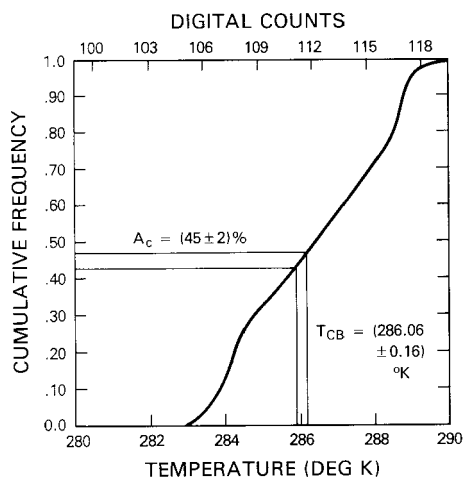

Figure 4c). Cumulative distribution of temperatures for the same 45% cloud-covered subscene used in Fig. 4a). This gives the fraction of pixels colder than a given temperature. Setting this equal to the cloud fraction determines the cloud base temperature, $T_{cb} = 12.9°C$.

two extremes, but as the resolution is refined to 120 m, narrowing the field-of-view to keep the number of pixels the same, the points spread out uniformly between the cloudy and clear clusters. This is due to the fact that the field of view is focusing in on the stratocumulus boundary, where a high percentage of partially cloudy pixels occur.

FRACTAL STRUCTURE OF FAIR WEATHER CUMULUS AND STRATOCUMULUS

Following the seminal work of Lovejoy (1982), the fractal structure of hail clouds was determined by Rhys and Waldvogel (1986) and of fair weather cumulus, stratocumulus, and deep convective clouds by Cahalan and Joseph (1989; see also Cahalan, 1983; 1988; 1989; Wielicki and Welch, 1986; Joseph and Cahalan, 1988). Much of the previous analysis focused upon marine clouds simply because cloud discrimination is much easier over the dark ocean background. However, this meant that there were little *in situ* data to verify the results. This situation has been remedied for boundary-layer clouds by the FIRE observations. Here we focus upon the analysis of the 7 July 1987 TM scene, especially subscenes a and b, described in the previous section, and the transition zone separating the two.

In this section we use data from the Electra fast-response temperature probe to confirm the TM estimates of cloud-base temperature, and verify previous results of cloud area and perimeter distributions. In the next section we show that TM observations of the structure of cloud reflectivity are related to the structure of cloud liquid water.

Cloud Base Temperature Threshold

In order to differentiate cloudy and noncloudy areas in a given band of a Landsat scene, we must determine a cloud base threshold for that band, which may differ from one scene to the next. A minimum requirement is that the threshold must produce the correct cloud fraction. For boundary-layer clouds such as those considered here, the cloud fraction may be determined from the thermal band by the spatial coherence method (Coakley and Bretherton, 1982), and the threshold then chosen to reproduce that fraction. Note that this threshold is simply the one required to reproduce the given cloud fraction, and is independent of assumptions about the emissivity near cloud edges. Here we shall see that the resulting cloud base temperature agrees well with the saturation temperature estimated from the *in situ* aircraft data for the 7 July FIRE scene.

The spatial coherence approach assumes that partially cloudy pixels have a radiance which is a

linear combination of the cloud top radiance and the surface radiance. Since radiance is approximately linear in brightness temperature over the range of interest, we have

$$T(i) = A_c(i)T_c + [1 - A_c(i)]T_s, \qquad (1)$$

where $A_c(i)$ is the cloud fraction for the ith pixel, or array of pixels, and T_c and T_s are the cloud top and surface brightness temperatures, respectively. This requires that we neglect variations in cloud emissivity and cloud height. Figure 4b) shows a spatial coherence scatter plot—mean vs. standard deviation of 4×4 pixel arrays—for a 128×128 subscene on 7 July in the transition region at the edge of the stratocumulus. The two clusters of points having minimum variance, one at the minimum temperature and one at the maximum temperature, arise from completely cloud-covered and cloud-free pixel arrays, respectively, and determine the cloud-top and sea-surface temperatures, giving

$$T_c = 10.55°C, \qquad T_s = 15.65°C. \qquad (2)$$

Averaging Eq. (1) over the pixel arrays allows us to solve for the mean cloud fraction in terms of the average temperature, and using (2) we obtain:

$$A_c = (T_s - T_{av})/(T_s - T_c) = (45 \pm 2)\%, \qquad (3)$$

where the 2% uncertainty in A_c is computed from the width of the T_s and T_c clusters in Fig. 4b). The appropriate "cloud base" threshold can now be determined such that it reproduces the cloud fraction A_c. This is done graphically in Fig. 4c), which shows the cumulative temperature distribution, i.e., the fraction of pixels colder than a given threshold temperature, vs. the threshold. Setting the fraction equal to A_c gives a cloud base threshold temperature given by

$$T_{cb} = (12.9 \pm 0.16)°C. \qquad (4)$$

Note that we have neglected any atmospheric correction in the above. In order to compare these remote sensing estimates with the *in situ* measurements, we consider a sounding, shown in Fig. 5, taken 1 h later in the same region by the NCAR Electra top-mounted dewpoint thermometer and fast-response temperature sensor. (Note that the altimeter-measured altitude shown here is less accurate than that given by the hydrostatic relation.) The cloud-top temperature measured by the Electra is $0.55°C$ warmer than the Landsat estimate, and the surface temperature is $0.85°C$ warmer, as expected from our neglect of atmospheric correction in the Landsat estimates. The correction is
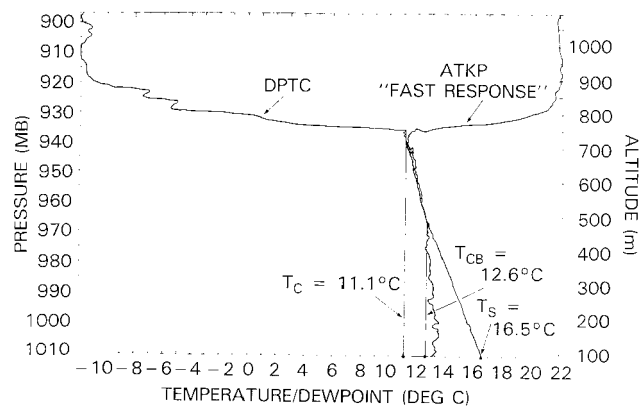

Figure 5. Sounding taken by the NCAR Electra across the stratocumulus boundary beginning at 1900 GMT, based on data provided by P. Austin. The temperature decreases adiabatically from the surface value of $T_s = 16.5°C$ until it reaches the dewpoint temperature at cloud base, where $T_{cb} = 12.6°C$, after which it decreases more slowly until it reaches the inversion, near the cloud top temperature $T_c = 11.1°C$.

relatively small because of the extreme dryness of the atmosphere above the inversion. In the moist tropical atmosphere the correction can be $6-7°C$, while $1-2°C$ is more typical of midlatitudes (see, for example, Wukelic et al., 1985). The cloud base temperature is within 2σ of the Landsat estimate. The slight warm bias in the cloud-base estimate may be due to a slight overestimate of A_c arising from the underestimate of $T_s - T_c$. However, the agreement of T_{cb} with the saturation temperature is remarkably good, especially considering that the brightness temperature near the cloud edges, where T_{cb} is being tuned to reproduce A_c, is rather poorly defined since the emissivity is varying.

It is important to note that the emissivity-weighted cloud fraction determined by the spatial coherence method may well underestimate the fractional area containing cloud liquid water. This difference could be significant if a large number of pixels contain low, but nonzero, optically thin liquid water. However, the cloud areas observed by Landsat appear to have similar fractal properties to the integrated liquid water observed during FIRE.

Coakley and Beckner (1988) have carried out extensive spatial coherence analyses on 60 km subscenes of the 1 km resolution AVHRR. Table 2 compares the TM results from Fig. 4a) with their results for a nearby subscene of Fig. 1 and with the *in situ* results from Fig. 5. Note that the bias

Table 2. Comparison of Cloud-Top and Sea-Surface Temperatures Determined by AVHRR, Landsat Thematic Mapper, and the Electra Sounding of Fig. 5

Instrument	T_c (°C)	T_s (°C)	ΔT (°C)
AVHRR	10.21	14.33	4.1
LANDSAT TM	10.55	15.65	5.1
NCAR Electra	11.1	16.5	5.4

Source: From Coakley and Beckner (1988, subscene 6,6 p. 87).

in sea-surface temperature is 2.17°C for the AVHRR, compared to 0.85°C for the TM, the increase being largely due to the inability of the AVHRR to resolve fair weather cumulus like those shown in Fig. 3a) (Bernstein, 1982).

Areas and Perimeters

We now check that the 7 July data reproduce some of the known fractal properties of fair weather and stratocumulus clouds [in Cahalan and Joseph (1989), a study of more than 400,000 cloud areas in 41 Landsat scenes], so that the case study reported here may be taken as representative. The cloud base reflectance threshold for each reflected band may be determined in the same way as T_{cb}, by plotting the cumulative distribution of reflectances in that band, and setting the fraction equal to A_c. The image may then be converted to a binary cloud image (1's for cloud pixels, 0's elsewhere) as discussed in Cahalan and Joseph (1989). The resulting cloud areas are binned in terms of $\log(\sqrt{(\text{area})})$. Figure 6a) shows a histogram of the areas for subscene a, plotted as log(number of clouds) versus $\log(\sqrt{(\text{area})})$. The usual change in slope is seen at about 0.4 km, with a slope of -0.6 for the smaller clouds, and -2.3 for the larger ones—again typical numbers for fair weather cumulus clouds. We shall see below that such changes in slope are typically associated with forcing at particular wavenumbers, and the scale of the forcing in this case is set by the boundary-layer depth.

Individual clouds cannot be identified in the stratocumulus subscene, subscene b, which is essentially 100% cloud-covered. We focus instead on the darker and optically thinner regions, to which the mean optical properties of stratocumulus are particularly sensitive (Cahalan, 1989). The optically thick regions are excluded by choosing a "cloud top" threshold with a $0.1A_c$ fraction, and areas darker than that threshold are identified.
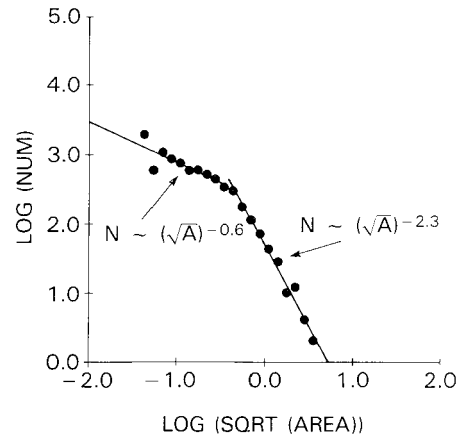

Figure 6a). Histogram of fair weather cumulus cloud areas for subscene a. The log of the number is plotted vs. $x = \log(\sqrt{\text{area}})$, and the bins are of equal width in x. The distribution is fit to two straight lines, with both the breakpoint and the slopes determined by minimizing the mean squared error. A clear change of scaling properties occurs at 0.4 km.
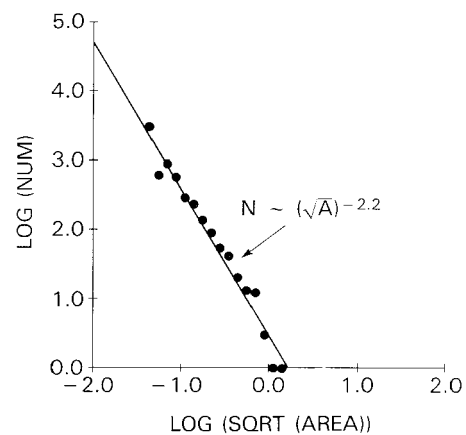

Figure 6b). Histogram of stratocumulus cloud "gaps" (regions of minimum reflectivity) for subscene b, plotted as in Fig. 6a). A single power-law $N(\sqrt{\text{area}}) \sim 1/(\text{area})$ appears to be a good approximation.

(This is an arbitrary choice, motivated by studies showing that most cloud liquid water is concentrated in 10% of convective clouds.) Figure 6b) shows the histogram of these dark areas or "gaps," plotted in the same way as Fig. 6a). A single slope fits the distribution quite well, and has a value close to that of the larger fair weather cumulus clouds.

Some measure of the roughness of these stratocumulus gaps may be obtained from the fractal dimension of their perimeters. Gaps which approximate some smooth analytic shape such as a rect-
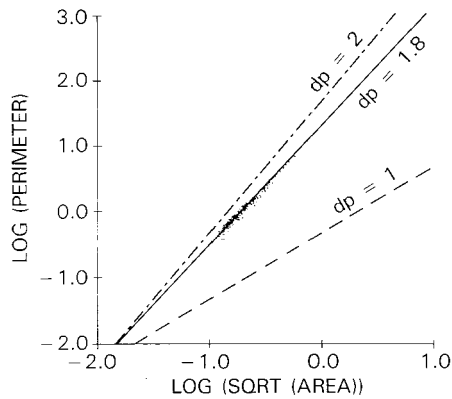
Figure 7. Perimeter — √area log–log scatter plot for the same stratocumulus "gaps" histogrammed in Fig. 6b). The least-squares straight line corresponds to a perimeter fractal dimension of $d_p = 1.8$, indicating highly irregular shapes.

angle or ellipse would have a perimeter fractal dimension close to 1. At the other extreme, gaps which take the form of long highly irregular "leads," which permeate all parts of the cloud field would have a perimeter fractal dimension close to 2. Figure 7 shows a scatter plot of the perimeter vs. √(area) for the gaps in subscene b. The least-squares straight line corresponds to a perimeter fractal dimension of $d_p = 1.8$, indicating highly irregular gaps which nearly cover the cloud field completely.

WAVENUMBER SPECTRA OF FAIR WEATHER CUMULUS AND STRATOCUMULUS

Our previous conclusions about cloud structure were based upon observations of cloud *reflectivity*, but a more basic question is how the cloud *liquid*

water is distributed, since the reflectivity can be computed from the distribution of liquid water, traditionally by specifying microscopic properties like drop sizes, and macroscopic properties like optical depth, etc. The radiation field provides a kind of low-pass spatial filter, so that there may be small-scale variations of liquid water to which the Landsat data are completely insensitive. However, we shall see in this section that certain aspects of the mesoscale structure of liquid water in stratocumulus are also observed in the Landsat reflectivity data. This structure is not included in our usual plane-parallel assumptions, and will be an important input to more realistic radiative transfer computations.

Integrated Liquid Water

Figure 8 shows a time series of 1-min averages of total vertically integrated liquid water measured at San Nicolas Island on 7 July 1987. Similar time series are available each day for 1–19 July. One of them (17 July) shows a pattern typical of fair weather cumulus: brief isolated high values separated by longer periods of low values. The other days are more similar to the 7 July stratocumulus case shown here. There are 5-min gaps every 4 h when calibration runs are done, and a few longer gaps due to system maintenance, but the record is otherwise continuous. Water vapor data are available, but are not considered here.

For each day separately we compute the frequency spectrum $S(f)$ by performing a fast Fourier transform (FFT) on the data, and squaring the resulting amplitudes. This gives the power in the

Figure 8. Time series of 1-min averages of vertically-integrated liquid water measured by upward-looking three-channel microwave radiometer on San Nicolas Island on 7 July 1987.
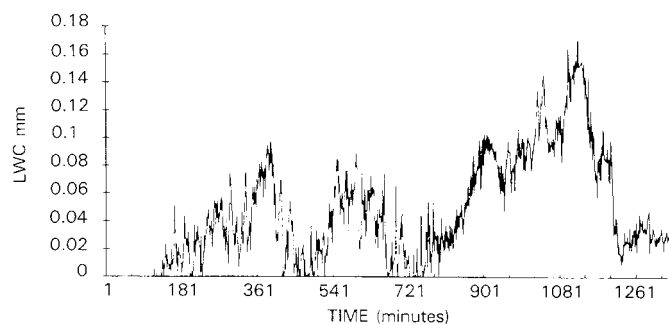
frequency range

$$1/\text{day} \leqslant f \leqslant 0.5/\text{min}, \qquad (5)$$

where 0.5/min is the Nyquist frequency. This may be converted to wavenumber by assuming frozen turbulence. That is, we assume that the variations seen at the tip of San Nicolas Island are due primarily to the advection of the spatial pattern of the turbulent liquid water field across that point, rather than to the local time dependence of the field. Then we can use the relation $v = \lambda f$, where v is the advection velocity, which we shall take to be 5 m/s, and λ is the wavelength, related to the wavenumber k by $k = 2\pi/\lambda$. This gives us the wavenumber spectrum $S(k)$ for wavelengths in the range

$$[5 \text{ m/s}/(1 \text{ day}) = 432 \text{ km}]$$
$$\leqslant \lambda \leqslant [5 \text{ m/s}/(0.5/\text{min}) = 0.6 \text{ km}]. \quad (6)$$

We have chosen seven days of data having gaps only during the 5-min calibration intervals, and these gaps were filled in by linear interpolation.

The spectrum for each day is computed as explained above, and the results are averaged, and shown on a log–log plot in Fig. 9. Also shown is a straight line with slope $= -5/3$, which is equal to the slope of the least-squares fit to the spectrum, so that to a first approximation we have

$$S(k) \sim k^{-5/3}. \qquad (7)$$

Figure 9. Spectrum of vertically integrated liquid water for 6 days of data similar to Fig. 8, converted from frequency to wavenumber assuming frozen turbulence with a mean 5 m/s advection. The least-square fit gives a 5/3 power-law decrease, suggesting that the liquid water fluctuates with the vertical velocity and may be treated as a passive scalar for the scales shown.
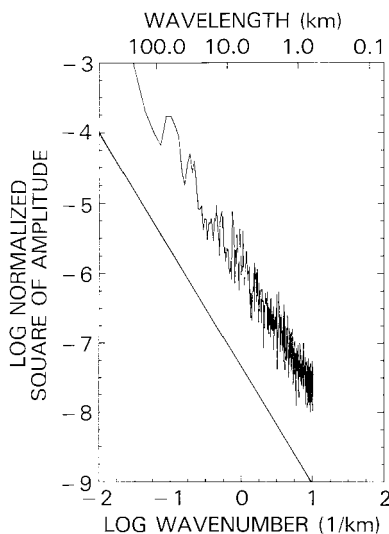
This is the classic Kolmogorov result for the wavenumber spectrum of any component of the velocity field, and is also the spectrum expected for a "passive scalar," i.e., a scalar field whose variations in space and time are due only to advection. This suggests that the total integrated liquid water in stratocumulus clouds fluctuates with the vertical velocity, being large in updrafts and small in downdrafts. This kind of behavior has been observed in fine-resolution numerical simulations (MacVean and Nicholls, 1988), though they do not reproduce the highly irregular fractal structure described in the preceding section. Correlations of vertical velocity and liquid water will be of much interest as more of the FIRE data becomes available.

TM Reflectivity

If the droplet density were varied while cloud geometry and microphysics were held fixed, one would expect cloud reflectivity to vary directly, and nonlinearly, with liquid water content. While this picture is undoubtedly oversimplified, it is interesting to compare the spatial structure of these two quantities. The wavenumber spectrum of fair weather cumulus and stratocumulus reflectivity can be determined directly from the Landsat data. We computed the spectrum of Band 2 for 10 horizontal scan lines spaced uniformly over the two subscenes shown in Figs. 3a) and 3b), and averaged the results. Figure 10a) shows the result for the fair weather cumulus subscene. As expected from the cloud size distribution [Fig. 6a)], there is a change of scaling properties near 1/2 km. The smaller scales, associated with variations within individual convective cells, follow a k^{-3} power law, expected for three-dimensional turbulence of a passive scalar, while the larger scales follow a much flatter $k^{-0.6}$, a nearly wavenumber-independent (white noise) spectrum. Unfortunately, insufficiently clear weather occurred on the island to obtain a comparable fair weather cumulus liquid water spectrum.

Figure 10b) shows the wavenumber spectrum of Band 2 in the stratocumulus cloud field corresponding to subscene b. Note that the spectrum for scales smaller than about 200 m follows a $k^{-3.6}$, similar to the fair weather cumulus, while the spectrum at larger scales follows the same $k^{-5/3}$ law seen in the liquid water spectrum in Fig. 9.
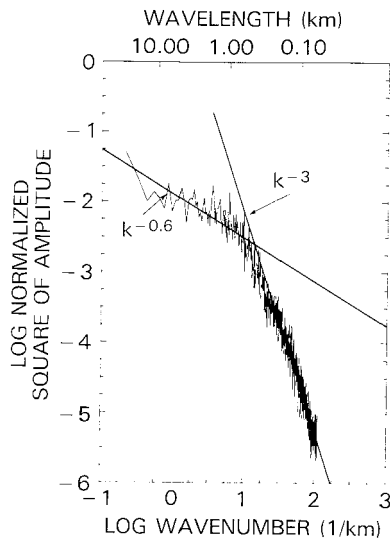
WAVELENGTH (km)

LOG NORMALIZED SQUARE OF AMPLITUDE

LOG WAVENUMBER (1/km)

Figure 10a). Wavenumber spectrum of TM Band 2 reflectivity in fair weather cumulus averaged over 10 scan lines of subscene a. As expected from Fig. 6a), there is a change of scaling properties near 1/2 km. The smaller scales follow a k^{-3} power-law, expected for three-dimensional turbulence of a passive scalar, while the larger scales approach a flat white noise spectrum.

WAVELENGTH (km)

LOG NORMALIZED SQUARE OF AMPLITUDE
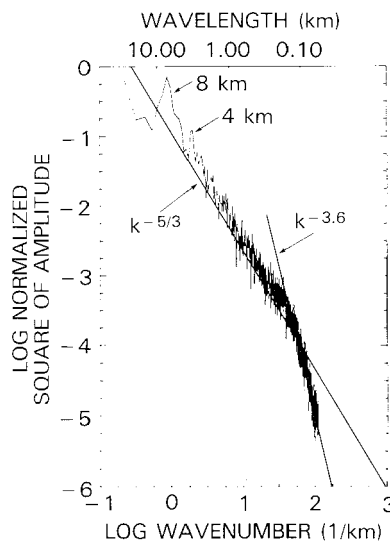
LOG WAVENUMBER (1/km)

Figure 10b). Wavenumber spectrum of TM Band 2 reflectivity in stratocumulus averaged over 10 scan lines of subscene b. The scales smaller than about 200 m follow a $k^{-3.6}$, similar to the fair weather cumulus, while the larger scales follow the same $k^{-5/3}$ law seen in the liquid water in Fig. 9. Peaks at 4 and 8 km correspond to the cloud streets seen in Fig. 3b).

Thus at least for the larger scales we expect a direct correlation between reflectivity and liquid water, though details of the structure of the two fields will likely differ. The reflectivity spectrum also shows peaks at 4 and 8 km corresponding to the cloud streets seen in Fig. 3b). These streets appear as a dominant feature to the human eye,

since the eye has selective detectors for linear features, but are no more important in terms of spectral power than the $k^{-5/3}$ background spectrum.

The type of break seen in Fig. 10b) is expected in two-dimensional homogeneous turbulence (Kraichnan, 1967). Energy is input at the cloud-thickness scale (200 m), and cascades downward in wavenumber, producing a $-5/3$ range, while the squared vorticity cascades upward to the dissipation range, producing a -3 range. Spectra of wind and temperature from commercial aircraft (Gage and Nastrom, 1986) show a -3 extending down from the 1000 km baroclinic forcing scale, and change to $-5/3$ at a few hundred kilometers, continuing to the smallest observed scale of a few kilometers. The stratocumulus brightness spectra suggest another change to -3 at small scales associated with convective forcing. It will be interesting to see if this break occurs in stratocumulus liquid water. A liquid water spectrum from a single cumulus cloud (King et al., 1981) gives a power of -1.8 down to a few meters. Perhaps the -3 is not found in such rapidly evolving clouds because the cloud thickness scale is not well-defined as it is in stratocumulus.

CONCLUSIONS

We have provided a detailed study of cloud spatial structure in the California stratocumulus regime with the help of data from the FIRE Marine Stratocumulus Intensive Field Observations, focusing on the 7 July 1987 Landsat Thematic Mapper scene. We have shown that the surface, cloud base, and cloud top temperatures determined by spatial coherence analysis of the TM thermal band are validated by the *in situ* aircraft soundings. The agreement is especially close for the cloud base threshold, upon which previous fractal studies are based. We have contrasted the fractal properties of the fair weather cumulus and stratocumulus subscenes of the 7 July scene. The fact that such divergent spatial structures are observed in close proximity underscores the potential "mixing" which can lead to misleading results in the analysis of coarse-resolution meteorological data. We have emphasized the importance of the darker, optically thinner regions which permeate the stratocumulus subscene. Comparison of the wavenumber spectra

in this subscene with that of integrated liquid water observed at San Nicolas Island suggests that the larger-scale brightness variations are associated with liquid water variations, and that these in turn are associated with variations in vertical velocity. (Insufficient data exist for a similar comparison in the fair weather cumulus.) This suggests that the dark fractal filigree seen in Fig. 3b) provides a picture of stratocumulus downdrafts. Verification of this will require further analysis of the FIRE observations of liquid water and vertical velocity.

Both the liquid water and the Landsat brightness spectrum follow the familiar $-5/3$ power law, whereas the fair weather cumulus brightness spectrum has a much flatter -0.6 power. Both cloud types follow a -3 spectrum for scales smaller than a few hundred meters. We have related the break in the stratocumulus brightness spectrum at 200 m to convective forcing at the scale of the cloud thickness, following Kraichnan (1967). It will be important to see if this break also appears in the liquid water, which will require analysis of both ground-based and aircraft high frequency data.

Simulations of fair weather cumulus and stratocumulus clouds have been developed which take some of the fractal properties into account. The simulated clouds are being used to determine the radiative properties of fractal clouds, and investigate the limits of plane-parallel theory. Monte Carlo radiative transfer computations have been carried out initially with a highly simplified model in which liquid water is redistributed in an initially plane-parallel cloud while cloud height and mean optical depth are held fixed at each step (Cahalan, 1989). Redistribution invariably decreases the mean albedo from the plane parallel case, since the albedo of optically thick regions saturates as optical depth is increased. The albedo of each homogeneous region may be computed from the thickness of each region independently only when the horizontal optical depth is large compared to the photon mean free path. The albedo of a region comparable in horizontal optical depth to the photon mean free path depends upon radiation from the sides. The mean albedo is insensitive to variations in optical depth on horizontal scales much smaller than the photon mean free path. Further development of these concepts will be closely tied to realistic simulations of the turbulent structure of boundary-layer clouds observed during FIRE.

Much remains to be done with the extensive FIRE data base. Aspects of the Landsat brightnesses may be related not only to variations in liquid water and vertical motions as discussed here, but also to changes in drop sizes, such as those associated with ship tracks, dynamical effects such as gravity waves or solitons, and variations in entrainment rates due to inhomogeneities in shear or buoyancy.

REFERENCES

Albrecht, B. A., Randall, D. A., and Nicholls, S. (1988), Observations of marine stratocumulus clouds during FIRE, *Bull. Am. Meteorol. Soc.* 69:618–626.

Austin, P. H., and Boers, R. (1988), Comparison and calibration of NCAR Electra instruments, *Proceedings of FIRE Science Team Workshop*, 11–15 July, Vail, CO, pp. 385–387.

Bernstein, R. L. (1982), Sea surface temperature estimation using the NOAA 6 satellite Advanced Very High Resolution Radiometer, *J. Geophys. Res.* 87:9455–9465.

Boers, R., and Betts, A. K. (1988), Saturation point structure of marine stratocumulus clouds, *J. Atmos. Sci.* 45:1156–1175.

Cahalan, R. F. (1983), Climatological statistics of cloudiness, invited paper in *Proceedings of 5th Conference on Atmospheric Radiation*, Baltimore, MD, October, pp. 206–213.

Cahalan, R. F. (1988), LANDSAT observations of fractal cloud structure, in *Scaling, Fractals and Nonlinear Variability in Geophysics* (D. Schertzer and S. Lovejoy, Eds.), Kluwer, forthcoming.

Cahalan, R. F. (1989), Overview of fractal clouds, in *Advances in Remote Sensing Retrieval Methods*, Deepak Pub., pp. 371–388.

Cahalan, R. F., and Joseph, J. H. (1989), Fractal statistics of cloud fields, *Mon. Weather Rev.*, 117:257–268.

Clark, B. P. (1986), New look-up tables, EOSAT Landsat Technical Notes No. 1, pp. 2–3.

Caughey, S. J., Crease, B. A., and Roach, W. T. (1982), A field study of nocturnal stratocumulus II. turbulence structure and entrainment, *Quart. J. Roy. Meteorol. Soc.* 108:125–144.

Coakley, J. A., Jr., and Beckner, M. H. (1988), Spatial Coherence retrievals of cloud properties for the FIRE marine stratocumulus IFO, NCAR Technical Note TN-307, 205 pp.

Coakley, J. A., Jr., and Bretherton, F. P. (1982), Cloud cover from high-resolution scanner data: detecting and allowing for partially filled fields of view, *J. Geophys. Res.* 87:4917–4932.

Gage, K. S., and Nastrom, G. D. (1986), Theoretical interpretation of atmospheric wavenumber spectra of wind and temperature observed by commercial aircraft during GASP, *J. Atmos. Sci.* 43:729–740.

Harshvardhan and Randall, D. A. (1985), Comments on "The parameterization of radiation for numerical weather prediction and climate models," *Mon. Weather Rev.* 113:1832–1833.

Harshvardhan and Weinman, J. A. (1982), Infrared radiative transfer through a regular array of cuboidal clouds, *J. Atmos. Sci.* 39:431–439.

Hartmann, D. L., and Short, D. S. (1980), On the use of earth radiation budget statistics for studies of clouds and climate, *J. Atmos. Sci.* 37:1233–1250.

Hogg, D. C., Guiraud, F. O., Snider, J. B., Decker, M. T., and Westwater, E. R. (1983), A steerable dual-channel microwave radiometer for measurement of water vapor and liquid in the troposphere, *J. Clim. Appl. Meteorol.* 22:789–806.

Joseph, J. H., and Cahalan, R. F. (1988), Nearest neighbor spacing in fair weather cumulus as inferred from LANDSAT, *J. Clim. Appl. Meteorol.*, submitted.

King, W. D., Maher, C. T., and Hepburn, G. A. (1981), Further performance tests on the CSIRO liquid water probe, *J. Clim. Appl. Meteorol.*, 20:195–202.

Kraichnan, R. H. (1967), Inertial ranges in two-dimensional turbulence, *Phys. Fluids* 10:1417–1423.

Lovejoy, S. (1982), Area-perimeter relation for rain and cloud areas, *Science* 216:185–187.

MacVean, M. K., and Nicholls, S. (1988), A fine-resolution, two-dimensional numerical study of a cloud-capped boundary layer, *Proceedings of the 10th International Cloud Physics Conference*, Bad-Hamburg, FRG, 15–20 August, pp. 425–427.

McKee, T. B., and Cox, S. K. (1974), Scattering of visible radiation by finite clouds, *J. Atmos. Sci.* 31:1885–1892.

Miller, E. R., and Friesen, R. B. (1987), Standard output data products from the NCAR research aviation facility, NCAR Research Aviation Facility Bulletin No. 9.

Ohring, G., and Clapp, P. (1980), The effect of changes in cloud amount on the net radiation at the top of the atmosphere, *J. Atmos. Sci.* 37:447–454.

Rhys, Franz S., and Waldvogel, A. (1986): Fractal shape of hail clouds, *Phys. Rev. Lett.* 56:784–787.

Snider, J. B. (1988), Estimated accuracy of ground-based liquid water measurements during FIRE, *Proceedings of FIRE Science Team Workshop*, 11–15 July, Vail, CO, pp. 289–292.

Stephens, G. L. (1976), The transfer of radiation through vertically non-uniform stratocumulus clouds, *Cont. Phys. Atmos.* 49:237–253.

Stephens, G. L. (1985), Reply (to Harshvardan and Randall), *Mon. Weather Rev.* 113:1834–1835.

Welch, R. M., and Wielicki, B. A. (1985), A radiative parameterization of stratocumulus cloud fields, *J. Atmos. Sci.* 42:2888–2897.

Wielicki, B. A., and Welch, R. M. (1986), Cumulus cloud properties derived using LANDSAT satellite data, *J. Clim. Appl. Meteorol.* 25:261–276.

Wukelic, G. E., Barnard, J. C., Petrie, G. M., and Foote, H. P. (1985), Opportunities and difficulties associated with using LANDSAT Thematic Mapper data for determining surface water temperatures, in *Racing into Tomorrow*, American Congress on Surveying and Mapping and American Society for Photogrammetry and Remote Sensing, pp. 879–891.